HHS Public Access

Author manuscript

Biomaterials. Author manuscript; available in PMC 2022 September 01.

Published in final edited form as:

Biomaterials. 2021 September ; 276: 121060. doi:10.1016/j.biomaterials.2021.121060.

Long-term *in vivo* two-photon imaging of the neuroinflammatory response to intracortical implants and micro-vessel disruptions in awake mice

Qianru Yang[1,2], **Alberto L. Vazquez**[2,3,4], **Xinyan Tracy Cui**[1,2,4]

[1]Department of Bioengineering, University of Pittsburgh, United States.

[2]Center for Neural Basis of Cognition, University of Pittsburgh and Carnegie Mellon University, United States.

[3]Department of Radiology, University of Pittsburgh, United States.

[4]McGowan Institute for Regenerative Medicine, University of Pittsburgh, United States.

Abstract

Our understanding of biomaterials in the brain have been greatly enhanced by advancements of *in vivo* imaging technologies such as two-photon microscopy. However, when applied to chronic studies, two-photon microscopy enables high-quality imaging only in superficial regions due to inflammatory responses introduced by the craniotomy and insertion of foreign biomaterials. Microprisms provide a unique vertical view from brain surface to ~1mm deep or more (depending on the size of the microprisms) which may break through this limitation on imaging depth. Although microprism has been used in the field of neuroscience, the *in vivo* foreign body responses to the microprism implant have yet to be fully elucidated. This is of important concern in broader applications of this approach, especially for neuroinflammation-sensitive studies. In this work, we first assessed the activation of microglia/macrophages for 16 weeks after microprism implantation by using two-photon microscopy in awake CX3CR1-GFP mice. The imaging window became clear from bleedings after ~2 weeks and the maximum imaging distance (in the horizontal direction) stabilized at around 500μm after ~5 weeks. We quantified the microglial morphology from week 3 to week 16 post-implantation. Compared to non-implant controls, microglia near microprism showed higher cell density, smaller soma, and shorter and less branched processes in the early-chronic phase. After week 5, microglial morphology further than 100μm from the microprism was generally similar to microglia in the control group. In

*Corresponding author: X. Tracy Cui, Ph.D., Department of Bioengineering, University of Pittsburgh, 5057 Biomedical Science Tower 3, 3501 Fifth Avenue, Pittsburgh, PA 15260, Ph: 412-383-6672, Fx: 412-648-9076, xic11@pitt.edu.

Qianru Yang: Conceptualization; Data curation; Formal analysis; Investigation; Methodology; Software; Visualization; Writing-original draft. **Alberto L. Vazquez**: Resources; Writing-review & editing. **X. Tracy Cui**: Funding acquisition; Project administration; Resources; Supervision; Writing-review & editing.

Declaration of interests

☒ The authors declare that they have no known competing financial interests or personal relationships that could have appeared to influence the work reported in this paper.

addition, time-lapse imaging confirmed that microglial processes were actively surveying by week 3, even for microglia at 50 μm. Our morphological and dynamic results suggest that microglia eventually exhibit normal phenotypes around chronically implanted microprisms. Next, we examined inflammatory responses after laser induced micro-vessel hemorrhage. Through the microprism, we captured microglia/macrophage polarization and migration, as well as reduced blood flow over an additional 16 weeks. To our surprise, microglia/macrophage aggregation around the insult site sustained over the 16-week observation period. This work demonstrates the feasibility of using microprisms for long-term characterizations of inflammatory responses to other injuries including implantable devices at deeper depths than that achievable by conventional two-photon microscopy.

Keywords

Two-photon imaging; microglia; blood brain barrier; microprism; brain inflammation

1. Introduction

An important and straightforward way to assess the performance of biomaterials is to test them on live animals and monitor the tissue responses over time prior to human applications. In vivo two-photon laser scanning microscopy enables imaging neuronal and glial activities in the brain of live animals with sub-micron resolution and sub-second scanning rate [1–5], which dramatically enhanced our understandings of physiological process and mechanisms of how neural tissue responds to biomaterials [6–8]. One of the greatest limitations of two-photon microscopy, however, is that the light scattering in a heterogeneous tissue, such as the brain, makes the image quality degrade quickly with increasing depth [9]. Therefore, two-photon microscopy has best imaging quality only in superficial brain regions. Moreover, except for retina [10], direct imaging of CNS usually involves surgical preparations such as cranial window or skull thinning [11, 12]. Biological complications like bone regrowth, meningeal thickening, and inflammatory cell infiltration can drastically deteriorate the imaging quality and depth. Although *in vivo* two-photon microscopy is able to reach ~600μm into the brain acutely [1–4, 13, 14], when there are foreign body responses in the brain, the imaging depth declines rapidly to 300 μm (layer II/III) within a week, and retains at around 150 μm thereafter [15]. Therefore, traditional two-photon microscopy generally unable to fulfill longitudinal evaluations of biomaterials in the deep cortex, where most of intracortical neural electrodes target to record and stimulate for neural circuit research or clinical applications [16–18].

Micro-prism implantation has provided a novel way of imaging the surface and the deep brain simultaneously [19, 20]. By reflecting the light on the slant surface of the micro-prism (1×1×1 mm glass prism), it presents a vertical view of the brain from the surface to ~1mm deep. Several studies have realized imaging vasculature, neuronal morphology, and calcium activities across all six layers of cortex in a single view [20–22]. Despite its great potential, concerns should not be overlooked that the surgical trauma and the inflammatory responses induced by the implanted microprism may confound the scientific questions being studied, as glial cells are essential for keeping homeostasis and normal neuronal functions [23–26].

A few histological studies indicate a low level of glial scarring at 27 days post implantation (DPI) [20, 27, 28]. However, microprism studies of brain inflammatory responses, especially those to different biomaterials, require a more careful and comprehensive characterization of the temporal evolution and extent of inflammatory responses induced by the microprism implantation itself. This is vital for the proper design and evaluation of inflammatory responses with minimal or no influence from the microprism. To evaluate inflammatory responses to microprisms in the brain, we used CX3CR1-GFP transgenic mice, a classic animal model of neuroinflammation and leukocyte trafficking. These transgenic animals express green fluorescent protein in microglia and peripheral monocytes, which can differentiate into macrophages and dendritic cells [29–31]. The physiological status of microglia is highly correlated with their morphology and behavior. In the normal brain, microglia continuously survey their surroundings with long, thin, and dynamic processes [32]. In pathological conditions, reactive microglia undergo drastic morphological and dynamic changes, such as sending processes toward the injury site, shortened and thickened processes, enlarged soma, and increased cell motility and proliferation [5, 33–36]. Two-photon microscopy has been successfully used by us and others to track the morphology and activity of CX3CR1-GFP cells with sub-micron resolution *in vivo*.

In the present study, we first characterized the evolution of the microglia response to microprism implantation by inserting microprisms into the somatosensory cortex of CX3CR1-GFP mice and tracking the inflammatory responses to the microprism device for 16 weeks. Quantification of microglial density and morphology as well as qualitative microglial mobility suggest that despite an acute activation of microglial reaction and proliferation near the microprism, the microglial phenotype eventually returned to homeostatic status after several weeks. After verifying that the microprism implant has no major chronic influences on the behavior of microglia/macrophages, we then characterized the inflammatory response to evoked microvascular injury as an example application of this microprism chronic imaging setup. We chose the laser-induced vascular injury model due to its capability to precisely target micro-blood vessels [29, 30, 37], and monitored inflammatory responses for another 16 weeks. Cerebral micro blood vessel injuries are very common in aged and diseased brains [38–40]. This type of injury may underlie cognitive dysfunction, but its pathological mechanisms remain to be carefully elucidated [7, 8, 41]. A recent study showed that micro-bleeds in superficial arteries trigger monocyte infiltration and microglial migration and proliferation [33, 42]. In this work, our results suggest that micro hemorrhages in deep cortex elicit not only acute microglial activation, but also long-term aggregation of microglia/macrophages in the ischemic core. Blood brain barrier (BBB) disruption is an essential challenge that invasive biomaterials often face in brain studies [43–45]. Revealing the consequences of BBB disruption could also provide insights to understanding the complex biological responses after implantation of biomaterials. This works serves as a proof-of-concept demonstration that this microprism implantation-based imaging model enables long-term evaluation of inflammatory responses to injury in the deeper regions of brain. In sum, we show the feasibility of using microprisms in CX3CR1-GFP mice for studies investigating inflammatory tissue responses to vascular injuries and biomaterial implantation in live animals chronically.

2. Methods

2.1. Microprism Assembly

The microprism was assembled following previous publication with minor modifications[19, 20]. The standard 1 mm borosilicate glass micro prisms were purchased from the Tower Optical Corporation(#MPCH-1.0). It has an aluminum coating on hypotenuse to deflect light beams at 90°. Three layers of coverglasses (#1 thickness, 0.15 ± 0.02 mm) were glued together using Norland Optical Adhesive 71 (NOA 71) and cured with ultraviolet light. The bottom two layers were 3×3 mm square coverglasses, and the surface layer was a 5mm diameter round coverglass (Warner Instruments LLC). The glass prism was then adhered to the bottom of the three layers of coverglasses with NOA 71 (Figure 1b).

2.2. Animals

Microprism implantation surgeries were performed on seven male B6.129P-Cx3cr1tm1Litt/J transgenic mice (The Jackson Laboratory, Bar Harbor, Maine). All animals were at the age of 10 to 20 weeks old at the time of microprism implantation. One animal (#2) died after one-week post-surgery, one animal (#4) had poor imaging quality because the prism detached from the coverglass soon after the surgery, thus their data were not used. The microprism device on animal #7 was coated with a zwitterionic polymer for a pilot study, so it was excluded from the analysis of inflammatory responses to microprism. All experimental protocols were approved by the University of Pittsburgh, Division of Laboratory Animal Resources and Institutional Animal Care and Use Committee in accordance with the standards for humane animal care as set by the Animal Welfare Act and the National Institutes of Health Guide for the Care and Use of Laboratory Animals.

2.3. Surgical procedure

Mice were anesthetized with a cocktail of ketamine(75mg/kg)/xylazine(10mg/kg) injected intraperitoneally (IP). The anesthesia status was maintained with periodic updates of ketamine(22.5mg/kg). After the hair was shaved off, mice were placed into a stereotaxic apparatus and above a heating pad. The head was cleaned with 70% isopropyl alcohol and betadine, and the skull was exposed. A rectangular stainless-steel chamber frame (#CF-10, Narishige International USA) was bonded to the skull with dental cement. The animal was then transferred to a stereotaxic frame that can hold the chamber frame. A 4×4 mm craniotomy was performed mainly over somatosensory cortex with a high-speed dental drill. The dura was carefully removed with fine forceps. A 1 mm long, 1 mm deep incision was made perpendicularly at the targeted region free of large surface blood vessels with a 28-gauge needle or a lance-shaped 0.1 mm thick razor blade (#72000, Electron Microscopy Sciences), manipulated by a stereotaxic arm. The exposed brain was rinsed with sterile saline and gently covered with wet Gelfoam until major bleedings stop. Then the blade was replaced with a vacuum line that suck up the surface coverglass of the microprism assembly with a blunt syringe tip. The microprism was slowly lowered into the brain, following the previous incision. Finally, when the prism was fully inserted, tiny drops of a silicone sealant (Kwik-sil, World Precision Instruments) were applied between the surface coverglass and brain to seal the window. The microprism assembly was further affixed to the skull with dental cement. The animals were treated with intraperitoneal (IP) injection of 5 mg/kg

ketofen (100 mg/ ml, Zoetis Inc., Kalamazoo, MI) and intramuscular (IM) antibiotic Baytril solution (10mg/kg BW, Henry Schein Inc.) for 3 days post-surgery.

2.4. Two-photon imaging

In vivo fluorescent images were acquired using a previously described two-photon laser scanning microscopic system[20–22, 46]. The components include a scan head (Bruker, Madison, WI), an ultrafast laser (Insight DS+; Spectra-Physics, Menlo Park, CA) tuned to a wavelength of 920 nm, non-descanned photomultiplier tubes (Hamamatsu Photonics KK, Hamamatsu, Shizuoka, Japan), and a 16X, 0.8 numerical aperture water immersion objective lens (Nikon Instruments, Melville, NY). Animals were IP injected with sulforhodamine 101 (SR101) (~0.05 cc; 1 mg/ml) right before imaging for visualization of blood vessels, and were head-fixed on a treadmill during imaging. For measurements of blood flow, two-photon line scans along the center of the target blood vessel were acquired at high frequency (0.8 to 2 kHz) [23–27]. Other than that, two types of images were collected: Z-stack images scan from the surface of the prism to the furthest imageable region over a field of view of 815 × 815 μm (1024 × 1024 pixels); ZT-series scans over a z-stack of 407.5 × 407.5 × 189 μm (512 × 512 × 63 pixels) were also continuously acquired for 15 to 40 min. The laser power was tuned linearly with z axis in order to partially compensate for the light loss in further areas, but was kept below 40 mW to avoid thermal damage.

2.5. Laser disruption of microvasculature

Photo disruption of microvasculature (point ablation) was created using the same laser source as two-photon imaging, but focused on a single point inside the vessel. The laser was tuned to 800 nm of wavelength, and point scanned at 1 kHz[20, 37]. The power and duration of the point scan started at around 10 mW for 1 s and were increased gradually until hemorrhage occurred or microglia being activated (extending processes). Live imaging was checked after each point scan session to assess the damage.

2.6 Post-mortem immunohistochemistry

Two animals (#5 and #6) were sacrificed at the end of the study for histology evaluations. After the animal was deeply anesthetized with 75mg/kg ketamine and 10mg/kg xylazine cocktail, we transcardially perfused the animal with 0.01M phosphate buffered saline (PBS) followed by 4% paraformaldehyde (PFA) in 0.01M PBS. The brain was extracted with the part of skull attached and the microprism in place, and post-fixed in 4% PFA in 0.01M PBS at 4 °C overnight. The tissue was then transferred to 0.01M PBS with 0.02% (w/v) sodium azide for storage at 4 °C. Before cryosection, the skull was carefully removed the brain tissue was truncated and soaked in 15% sucrose (Sigma-Aldrich Corp., St. Louis, Missouri) in 0.01M PBS with 0.02% (w/v) sodium azide at 4 °C until it sunk and then 30% sucrose solution in the same PBS-azide at 4 °C until it sunk. Later we froze the tissue in a cocktail of 2:1 20% sucrose in PBS: optimal cutting temperature compound (Tissue—Plus O.C.T. Compound, Fisher HealthCare, Houston, TX), immersed in an Isopentane bath in a box of dry ice. The frozen brain tissue was then sliced into 25 μm thick sagittal sections using a cryostat (Leica CM1950, Buffalo Grove, IL). The staining procedure was previously described [47]. We used FOX3/NeuN-Alexa Fluor® 350 conjugated antibody (1:300, bs-1613R-A350 Bioss), GFAP antibody (1:500, Z033401 Dako), iNOS antibody

(1:250, 482728 Millipore), Arginase-1 antibody (1:500, ABS535 Millipore), and TMEM119 antibody (1:300, ab209064 Abcam) to label neural nucleus, astrocytes, M1 macrophages, M2 macrophages, and resident microglia, respectively. The sections were imaged using a Nikon A1 Confocal Microscope at the Center for Biologic Imaging at the University of Pittsburgh.

2.7 Data processing

2.7.1. Z-stack image alignment and imaging depth characterization—Two-photon z-stack images were used for quantifications of imaging depth, surface encapsulation, microglia/macrophages density and soma size. The stack was rotated to align the prism surface to the x-y plane using the ‘interactive stack rotation’ function in ImageJ. For imaging depth characterization, the aligned stack was side projected to the y-z plane with the ‘3D project’ tool. We then measured the distance from prism surface to the most distal recognizable microglia as the imaging depth.

2.7.2. Surface encapsulation of microprism—Surface encapsulation of microglia/macrophages on the microprism surface was automatically assessed with a custom Matlab script. The thresholding algorithm was based on previous publications on analyzing microglial coverage of neural implants[7, 8, 20, 48]. Basically, after alignment, a 30μm thick stack image at the prism surface was projected into a 2D image. 15% of the margins were removed due to lack of illuminations, leaving the center region of the image for analysis. A threshold to distinguish signal from background was set at mean +1*SD. Next, a second threshold was set at mean+3*SD of the noise. The surface encapsulation percentage was calculated as the ratio of area above the second threshold over the whole analyzing area.

2.7.3. Density and soma size quantification—Using the aligned stack, multiple 30μm thick substacks were summed to form a 2D image in x-y plane with the ‘z project’ function in ImageJ. These substacks were centered at 50μm, 100μm, 200μm, 300μm away from the prism. Batch processing was achieved with a Macro script in ImageJ. We selected 200μm×200μm subregions in the brain parenchyma with good clarity and uniformity for the following analysis. The same region was tracked over time as closely as possible. We corrected the uneven background illumination by subtracting a Gaussian blurred image (sigma=20) from the original image. To extract the soma information, a bandpass filter was applied before administering a median filter and the ‘despeckle’ function. For particle analysis, a threshold was set at mean+2.5*SD of the processed image, followed by ‘despeckle’ and ‘watershed’. The above procedure was optimized based on manual supervision of several randomly picked sample images. Finally, we used the ‘analyze particles’ function to get the number of cells and the projection area of each cell. Based on these numbers, the density of microglia/macrophages was calculated.

2.7.4. Cell morphology analysis—The 200μm × 200μm two-photon images in 2.7.3 were also used here. An ImageJ Macro script was developed for automatic morphology analysis based on previous publications [49, 50]. Briefly, the images were first normalized by equalizing the histogram, and then an ‘unsharp mask’ was applied to make the processes structure prominent. After setting a threshold by ‘Otsu’ method, the binary image was fed

into ‘skeleton analysis’ to quantify the length of processes and the number of junctions. The average processes length and number of junctions per cell was calculated by dividing the number of cell bodies resulted from particle analysis in 2.7.3.

2.7.5. Blood flow speed measurement—Blood flow speed was measured in a similar manner as published studies [27, 28, 46]. Using the line scan acquisition, a fluorescent dye (SR101) was pre-injected to label the vasculature, such that red blood cells (RBCs) show as shadows flowing in the blood vessel. These line scans were stacked sequentially, forming a spatial(x)-temporal(t) image. The motion of RBCs results in dark streaks in the x-t image, therefore the moving speed of RBCs can be calculated based on the angle(θ) between these dark bands to the horizontal(x) axis:

$$v = \frac{\Delta x}{\Delta t} = arctan\theta \quad (1)$$

The laser scan rate was tuned to around 1ms per line to properly calculate the slope.

2.7.6. Ramification ratio of microglia—After the laser insults, a 30μm thick stack centering at the injury plan was projected to a 2D image for the ramification ratio analysis. Microglia were categorized into ‘ramified’ (1) or ‘polarized’ (0) on the basis of their morphology[6, 7, 27]. Basically, microglia that extend processes roughly equally in every direction were considered ‘ramified’ (1), while microglia that preferentially extend processes toward the insult were regarded as ‘polarized’ (0). After binning microglia by distance from the insult, we calculated the ramification ratio by averaging the categorical value of pooled microglia in all biological repeats. A Boltzmann sigmoidal model was used to fit the ramification ratio change over distance from the injury site.

2.7.7. CX3CR1-GFP intensity distribution—The same projection image mentioned in 2.7.6. was also utilized for the fluorescence intensity quantification. After cropping out the meningeal region, we binned the CX3CR1-GFP fluorescence intensity in every 25μm radius increase originating from the insult site. The averaged intensity value of each bin was normalized by subtracting the mean value of the two most distal bins. The 3D intensity distribution plot was generated in *Microsoft Excel* (Microsoft Office, Redmond, USA).

2.7.8. Statistical analysis—All statistical analysis was done with Prism software (GraphPad). Throughout the text, p-value were presented as *: $p<0.05$, **: $p<0.01$, ***: $p<0.001$, ****: $p<0.0001$.

3. Results

3.1. Experimental setup

In this study, we first assessed the recovery of microglia/macrophages after microprism implantations for 16 weeks. After the microprism device fully settled, we then tested the capability of microprisms for chronic investigations of inflammatory responses upon brain injuries by a laser-induced microvessel insult (Figure 1a). We followed previous publications for microprism assembly with minor modifications [19, 20, 37]. The implant consists of

three layers of coverglass (one 5mm round, two 3mm square) and a 1×1×1 mm right triangular prism, adhered together by an optical glue (Figure 1b). We made a 1mm long and 1mm deep coronal incision in the somatosensory cortex region, and carefully inserted the microprism assembly into the slot (facing the anterior side). Each 2D image taken through the prism is essentially an optical coronal section of the brain. When the objective of the two-photon microscopy comes closer to the brain, the imaging plane is moving farther away from the microprism along the z-axis (Figure 1b and c). The bottom layers of square coverglasses were in direct contact with the brain surface to prevent dura and bone regrowth underneath, thus allowed chronic imaging through the clear cranial window (Figure 1c). After the animal recovered from the surgery, we transferred it on a treadmill, with the head fixed by a metal frame that was attached to the skull (Figure 1c). Subsequent chronic two-photon microscopy images were all acquired when the mouse was awake on the treadmill

3.2. Vasculature remodeling and recovery after microprism implantations

CX3CR1-GFP mice were imaged on the day of surgery, 1-day post implantation (DPI), 3 DPI, 7 DPI and then weekly for 16 weeks. Variabilities on the spatial and temporal occurrence of bleeding at the brain surface were observed between animals, as the degrees of blood vessel disruptions resulted from the microprism implantations varied (Figure 2). In more than half of the animals, bleedings exacerbated in the first several days post-surgery, but stopped after ~2 weeks and the vascular pattern over brain surface retained stable thereafter. A fluorescent dye (SR101) was used to illuminate the vasculature, especially near the microprism imaging face. Vasculature remodeling, when observed, was most obvious between day3 to week2/3 post-implant at the microprism surface (Figure 2). After 3 weeks, the general vasculature remained stable, although minor remodeling may exist, such as subtle changes of the vascular curvature (Figure 2). Our observations are consistent with previous studies, in one of which the vasculature recovered and stabilized after around 15 days as revealed by visible-light optical coherence tomography [22], suggesting a good reproducibility of microprism implantations and that this setup is suitable for longitudinal studies on vasculature disorders.

3.3. Longitudinal imaging clarity after microprism implantations

Through the microprism, we took a z-stack of images from the surface of prism to the farthest visible tissue (Figure 3a). 30 μm thick sub-stacks at a series of distances are cropped out and averaged to 2D images in the x-y plane for further presentations and quantifications.

To quantify the imaging depth in the Z direction, we projected the 3D stack of images to the y-z plane. In the cortex of a healthy brain, microglia distribute near uniformly with moderate density [39, 40], which makes them an easy marker for evaluating imaging quality and depth than the layer-differentiated neurons. From the side projections, we measured the distance from the prism surface to the most distal observable CX3CR1-GFP cell. The horizontal direction imaging depth from all four animals followed a similar trend, which decreased from d0 (352.8±85.1 μm, mean ± SD) to d3 (143.2±22.7 μm, mean ± SD), then increased gradually, exceeded 400 μm at week 3, and stabilized at around 500μm after week 5 (Figure 3b&c). At 500 μm from the microprism, fine structures such as microvascular and

microglial processes are still identifiable, although week 16 showed slightly higher noise than week 3 (Figure 3d). Before week 3, brain regions that are equal or farther than 50 μm from the microprism were partly dark and blurry (Figure 3b, supplementary figure 1), likely due to insertion induced bleedings and cell death. Clear and stable images were observed from week 4 to week 16 (Figure 3b, supplementary figure 1), which suggested that the tissue largely recovered in 4 weeks. The accessible depth of brain tissue in the vertical direction is defined by the size of the microprism. Here the 1mm microprism enabled chronic imaging of vasculature and microglial morphology from the brain surface to ~800 μm deep (supplementary figure 1), allowing for observations of superficial cortex and deep layers simultaneously, which is a drastic improvement from the conventional two-photon microscopy.

3.4. Foreign body responses to microprism implantations

Previous studies of the foreign body responses to intracortical implants have been massively focused on neural electrodes. A dense glial scar accompanied by neural loss and degeneration is found up to about 200μm from chronically implanted microelectrodes [36, 51, 52]. The microglial coverage to acutely implanted Michigan-style silicon micro-electrode arrays (4 shanks, each implanted part is 600 μm long, 15 μm thick, 30–55 μm wide) is about 40% as quantified by our group [7, 8]. Here, the microglial/macrophage coverage at the microprism surface stayed at a much lower value around 10% (Figure 3e&f), quantified using the same method.

In addition, at the end of this study (~32 weeks post microprism implantation), we extracted the brain tissue for post-mortem histology. Since it was difficult to remove the coverslips and prism implants without causing damage to the prism/tissue interface, we were only able to obtain two brains with well-preserved tissue interface for immunohistochemistry. In situ immunohistochemistry and tissue clearing techniques could be used for ex vivo examination of the interface [53, 54], however due to concerns over tissue expansion and deformation we decided not to attempt this procedure. The tissue responses observed were similar between the two animals and the images shown are representative. The brains were sectioned sagittally, perpendicular to the microprism imaging surface. Qualitatively, astrocytes (GFAP) fluorescence was elevated up to around 100 μm from the microprism, along with a decrease of neuronal (NeuN) density (Supplementary figure 2). The microglial distribution does not appear denser than background beyond 10 μm of the microprism surface, and all CX3CR1-GFP cells are co-labeled with a resident microglia marker (TMEM119) (Supplementary figure 2). iNOS (proinflammatory macrophage marker) and Arginase-1 (anti-inflammatory macrophage marker) co-localized more in microglia near the microprism (<300 μm), while distant microglia are prone to be labeled by just Arginase-1 (Supplementary figure 2).

Taken together, there is a highly confined chronic foreign body response to microprism implants. comparable or milder than traditional intracortical microelectrode arrays.

3.5. Detailed evaluation of microglial morphology after microprism implantations

To characterize the recovery progress to microprism implants *in vivo*, we quantified the morphology of microglia over time. Because of bleedings and limited imaging distance in

the early period, we analyzed images from week 3 to week 16. Particle analysis quantifies the number (density) and size of microglial soma, while skeleton analysis characterizes the length and number of junctions for microglial processes (Figure 4). Compared to no implant acute craniotomy controls, microglia close to the microprism showed significantly higher density, smaller soma size, shorter processes, and reduced number of processes junctions in the early phase (Figure 4 & 5). The increase in density and the decrease in the length and junctions of processes indicate activated microglia. The smaller soma size is unexpected but could be explained by microglial proliferation. From week 3 to week 16, the processes length and junctions per cell at ≥100 μm were similar to the control (Figure 5). After week 5, microglial density and soma size at ≥100 μm were not different from the control in general (Figure 5). At 50 μm from the microprism, all the morphology characterizations turned to the same level of control after week 12 (Figure 5). These results suggest that future neuroinflammation studies involving characterizing microglial morphology should consider 5 weeks of recovery if imaging at ~100 μm from the microprism or 12 weeks of recovery if imaging at ~50 μm.

Besides microglia, CX3CR1-GFP is also expressed in monocytes and infiltrated macrophages in the brain. Using the microprism implantation setup, we were able to identify these types of cells in a vertical view, according to their characteristics described in previous studies [20, 42]. From 3D time lapse images acquired by *in vivo* two-photon microscope, we presented the morphology and motile abilities of these cells at 50μm away from the prism device with temporal coded color (Figure 6, supplementary movie 1). Microglia are the most abundant $CX3CR1^+$ cells in the brain parenchyma. In the first several days after surgery, microglia showed an enlarged cell body with short and thick processes, a typical phenotype of microglial activation (quantification was difficult over this period due to poor imaging quality). After week 4, microglia turned back to small soma with thin and highly mobile processes, suggesting that these microglia were surveilling their environment. The small and round $CX3CR1^+$ cells in the blood vessels are assumed to be the circulating monocytes. They are not frequently seen in 3D time lapse two-photon images probably due to their fast movements. Meningeal macrophages were absent in the beginning due to the removal of dura during the microprism implantation surgery. They appeared at the surface of brain as early as day 3 post-surgery. After 2 weeks, meningeal macrophages aligned in the horizontal plane, suggesting the reestablishment of a new sealant at the brain surface (supplementary movie 1). Foam-like giant phagocytic macrophages were found sweeping near the prism surface at day 3 post-surgery, and missing after week 2, indicating an active debris-cleaning period of phagocytic macrophages in the first two weeks (supplementary movie 1). Collectively, our results above suggested that although there was a short-term activation of microglia and macrophages near the prism, the inflammatory responses largely settled down by week 2/3. And from week 4 to week 16, the dynamics behaviors of all the above $CX3CR1^+$ cells were generally stable and that microglial motilities were similar to that imaged through a thinned skull cranial window, proving the feasibility of using prism implantation for dynamic inflammatory studies *in vivo*.

3.6. Long-term monitoring of inflammatory responses to microvascular insults

So far, our results suggest that microglial morphology and dynamic activities both restore after 4–12 weeks of implantations at ≥50μm from the microprism face. Next, to test whether we can apply this microprism setup to study chronic inflammatory responses in the cortex, we induced micro vascular insults as described in previous publications [29, 30, 37]. This injury model can create micro-scale vessel damage in a well-controlled manner, so excessive bleedings that may impede observations of inflammatory responses can be avoided. Additionally, breakage of micro-vessels is almost an inevitable challenge faced by invasive biomaterials. Thus, this work can provide insights for understanding the influence of blood vessel damage aside from other issues of neural implants.

800nm laser light was focused on a single point inside the target micro-blood vessel to introduce an ischemic injury. The power and duration of the laser light were started at low values (10 mW for 1 s at 1kHz) and increased gradually until we found signs of injury. In 3 of 4 animals, hemorrhagic ischemia of ~100μm in diameter were successfully generated, accompanied by leakage of intravascular dye, transient edema, and optical dark rings (Figure 7a, supplementary movie 2). This vasogenic edema is a common complication in a variety of disorders including strokes, brain tumors and brain trauma [37, 55, 56]. The blood flow quickly (<1h) diminished and remained significantly lower than the pre-injury level throughout our 16-week observation period (Figure 7b). Abundant microglia and microglial processes congregated around the damaged site in several hours (Figure 7a). The fluorescent intensity, a general indication of microglia/macrophage activation level, climbed gradually after the insult, reached the apex at day 3, and then shrank to a small region with a diameter of around 50μm after one or two weeks (Figure 7c). To quantify how far away the microglia responded by transforming into the polarized morphology, we calculated the ratio of ramified cells in the total population of microglia from all three animals and fitted Boltzmann sigmoidal curves to the plot of ramification ratio over distance (Figure 7d). The polarization radius (defined as the distance where the ramification ratio reaches 0.5 in the sigmoidal fitting) increased slightly from 1h to 4h post injury, and then dropped a little from 4h to 6h (Figure 7e). After one day, large number of CX3CR1-GFP cells emerged around the site of injury, but almost none of them showed obvious polarized processes (Figure 7a, d, e). Note that cell density quantifications were not conducted because of the difficulties to differentiate microglial pseudopodia from microglial soma and to count them in those aggregations. However, it was clear that microglia/macrophages density in the penumbra gradually decreased after one week, while a microglia/macrophages cluster retained at the ischemia core for over 4 months (Figure 7a, c, supplementary movie 2). The inflammatory responses were consistent in all three animals who experienced laser-induced hemorrhagic ischemia.

In two cases, we administered the same laser insulting method, but each time hemorrhage did not occur, even under high laser power and long pulse duration, while microglia had been activated (sending processes toward the insulted site). The outcome variability may result from micro-motion of the brain tissue that off target the laser. We ceased pushing the laser power but monitored inflammatory responses to this milder insult for 4 weeks. In several hours, the insulted site was wrapped by the pseudopodia of neighbor

microglia (Supplementary figure 3a). Except for several directly neighboring microglia, most microglia did not send processes toward the insult (Supplementary figure 3a). The local blood flow decreased in the first a few hours post-injury and recovered within one day (Supplementary figure 3b). The CX3CR1-GFP intensity increased in the first several hours post injury and returned to the baseline by week 2 (Supplementary figure 3c). These results drastically differ from the laser induced hemorrhagic injury, indicating that while point laser ablation itself could induce local and temporal microglial activation, the massive and chronic inflammatory responses are most likely related to the BBB breakage rather than the thermal damage.

3.7. Dynamics of microglia/macrophages after laser induced micro-hemorrhage

Before the laser insult, brain microglia showed ramified morphology with highly mobile processes and static soma, indicating a homeostatic surveilling state (Figure 8a). After hemorrhage was generated on a micro vessel, microglia sent out processes towards the damaged location in several minutes (Figure 8a). In an hour, we started to observe migration of microglial soma along the processes they paved (Figure 8a). The moving speeds of migrating microglial soma at <1h, 2h, 4h, 6h, day1 and day3 post injury were 1.81±0.59μm/min, 1.36±0.70μm/min, 2.26±1.16μm/min, 1.66±0.98μm/min, 1.37±0.70μm/min and 1.17±0.42μm/min (mean ± SD), respectively, all of which were significantly higher than non-activated microglia (0.21±0.13μm/min), except for day3 (Figure 8b). No significant difference was found between any two time points after the hemorrhage, indicating that the migration speed is time independent. Across all the listed time points, the moving speed of migrated microglia we observed was 1.70±0.95μm/min. From day7 and beyond, no obvious microglia migration was seen from our 15 min's imaging period (Figure 8a). Moreover, the distance of migrating microglia from the injury site at different time points were not significantly different from each other in our field of view (Figure 8c). We wondered whether the microglial migration speed is correlated with where they located, so we plotted the mean migrating speed of each cell as a function of the distance from the injury (Figure 8d). The linear fits at all time points had slopes close to 0 and R square less than 0.3, showing that the migration speed is unrelated with the microglia location. The number of migrating cells in the same view, however, did change over time (Figure 8e). From the three animals, we saw a quick increase in the number of migrating microglia in the first 6h post injury, followed by a relatively slow decline in several days (Figure 8e). Interestingly, we found some microglia migrating away from the injury since about 2 hours post hemorrhage. We calculated the mean moving direction index of each microglia over the observed migration period, whose value at individual time frame was determined by the following equation:

$$Direction\ \ index\ = \begin{cases} 1,\ \Delta d < 0 \\ 0,\ \Delta d = 0 \\ -1,\ \Delta d > 0 \end{cases} \quad (2)$$

where $\Delta d = d_{t+1} - d_t$ is the distance change between two consecutive time frames. For example, when the cell moves closer to the injury site, Δd<0, a direction index of 1 is then assigned to that time frame.

Therefore, a mean direction index of 1 means that the cell continuously moves towards the injury in the 15min observation, and −1 means that the cell keeps migrating away from the injury, and 0 means that the cell spend equal times on approaching or leaving the hemorrhage core. The retrograde microglia were first noticed at around 2h post injury (Figure 8f). Up to day1 post injury, the majority of microglia spent more times migrating towards the damaged site, while at day3, most microglia spent more times moving away from the injury (Figure 8f). We also plotted the ratio of migrating cells in the total microglia population to get an idea of the likelihood that microglia migrate at different distances and at different time points (Figure 8g). This analysis revealed a gradually increased migrating ratio at around 120–240μm from 1h to 4h post injury in this 407.5×407.5 μm field of view, and a decrease trend in that region from 6h to day3. In addition, all migrated microglia were seen within a 300μm distance (Figure 8g).

3.8. Microglial plasticity and degeneration

During imaging, we observed some novel microglial behaviors that have not been reported. In one case, we induced a second hemorrhage damage of a blood vessel at 5 hours after the first injury and at ~150μm away. Polarized microglia were still responsive to new damages. Specifically, microglia that were closer to the second damage retracted their former processes and projected new processes towards the second injury site by 20 min (Supplementary figure 4, supplementary movie 3). Meanwhile, microglia closer to the first injury remained polarized to the first damaged site. These findings suggest that the polarization of microglial processes is reversible, and that the direction of polarization is related to the distance from the injury. Another interesting observation was microglia degeneration near the hemorrhage (Supplementary figure 5, supplementary movie 4). The degenerating microglia pulled back their processes first, and then the fluorescent signal faded away within 30min after the hemorrhage. We confirmed that the microglia did not migrate to a different z plane but just disappeared in place. These qualitative observations raise awareness of microglia plasticity and degeneration, while profound understandings of these behaviors require future investigations.

4. Discussions

4.1. Inflammatory responses to the microprism implant

Although the morphology of microglia was first illustrated more than a century ago [57], people regarded microglia as static cells until *in vivo* two-photon microscopy imaging techniques revealed that microglia survey the surrounding environment with highly mobile processes at the so called ‘resting’ state [32]. Upon sensing damage, microglia respond quickly with series of morphological and molecular changes, depending on the severity of injury [33, 58]. A local brain injury such as focal laser insults or microelectrode insertions, trigger immediate movements of microglial processes toward the injury [5, 6, 55, 56]. Later on, microglia may proliferate and migrate to the insulted site from hours to several days post injury [33, 57]. More severe insults, for example, traumatic brain injuries, systemic infection and major neurovascular diseases, can induce larger microglial morphological transformations into amoeboid-like cells, rod-shaped cells, foamy phagocytic macrophages [59, 60], etc. As one of the first-line defensive cells in the brain, microglia present antigens,

and secret chemokines and cytokines to orient other immune cells [34, 58]. Molecular-level studies revealed diverse phenotypes of microglia, and that the microglia population may shift their profile from neuro-supportive to pro-inflammatory and neurotoxic in a short period after brain injury [5, 6, 61–63].

To our surprise, the microglial responses to the microprism implant (1mm ×1mm ×1mm) were comparable to microelectrodes, despite hundreds of times difference in size. Extensive studies have reported higher amount of microglial signal persisting around chronic intra-cortical microelectrodes [33, 47, 51, 64]. Specifically, at 4 weeks, Iba-1 immunostaining revealed a higher reactive microglia region that extend to 100~150μm around implanted microelectrodes [47, 51, 59, 60, 64]. By 8 weeks, that region shrank gradually to ~50μm [34, 64]. In this work, we observed higher density of microglia up to ~200 μm at 4 weeks; at 8 weeks, microglial density beyond 50μm also returned to the baseline level. The microglia surface coverage remained at ~10%, significantly lower than that on silicon microelectrode devices (~40% as observed in acute studies).

We speculate two potential reasons for the low level of inflammation to microprism as follows. First, although the relative larger volume of prism disrupts more blood supply and induces more initial trauma, it presents no sharp edges nor free cantilever end as in the case of micro neural electrodes. As a result, the tissue nearby experiences less micromotion induced injuries. Second, the material of the prism—silicate glass (BK-7: silica (70%wt), boron oxide (11.5%wt), sodium oxide (9.5%wt), potassium oxide (7.5%wt), barium oxide (1%wt), titanium oxide, calcium oxide and impurities in small quantities)—may well be in good biocompatibility with brain tissue. Many types of silicate glass have been widely used clinically in dental and bone applications demonstrating scar-free bone integration and ability to stimulate new bone growth [61–63, 65, 66]. This study provided an example of good brain tissue integration with silicate glass, which is worth further investigation to explore the applications of silicate glass material for intra-brain devices.

4.2. Pathology of the insults in micro blood vessels

The laser induced micro-blood vessel insults mimics pathological micro-ischemia and micro-hemorrhage in the brain. In clinical studies, the prognosis of intracerebral hemorrhage is much worse than ischemic strokes of similar sizes [47, 51, 64, 67–69]. Our preliminary data are consistent with these clinical observations. We found quick microglial polarization within several minutes and microglial migration in the first week post hemorrhage insult. These findings are corroborated by numerous previous studies without a microprism implant: in the penumbra region of focal cerebral ischemia, activated and proliferating microglia increase in the first week [35, 70]. Multiple acute in vivo two-photon microscopy studies observed immediate microglial polarization in response of injuries in the shallow brain regions [6–8]. Evidence of microglial migration and proliferation have been found near the brain surface after laser damage of a major penetrating blood vessel [33, 64]. However, the chronic microglial activation for over 16 weeks to a single capillary breach has not been reported before. This may be due to the lack of proper tools to track microglial responses in the deep brain for several months. Past two-photon microscopy work found an increase in CX3CR1-GFP intensity for one or two weeks after similar laser ablation of penetrating

blood vessel in layer II/III [71]. The location and the diameter of the insulted blood vessel may also contribute to different inflammatory responses, as the superficial tissue is more exposed to cerebrospinal fluid and peripheral macrophages, and that larger blood vessels are more difficult to be occluded. Micro-infarcts are frequently seen in asymptomatic elderly people, and are correlated with higher risk of stroke [72, 73]. Our data showed that a micro-hemorrhage triggers not only transient microglial polarization and migration, but also chronic microglial activation for over four months. This indicated that a micro-hemorrhage in deep cortex can induce long-term activation of the inflammatory system and may be related with other neurodegenerative diseases.

4.3. Blood flow speed and microglial scar

Mild ischemia and micro-hemorrhage showed different patterns of blood flow post insults. In the case of mild ischemia, the blood flow speed dropped gradually in 3 hours (Supplementary figure 3b). The time delay between the laser insult and the low blood flow speed implies an involvement of biological processes such as the platelet aggregation [65, 66, 74]. After 1 day, blood flow speed recovered, and became even higher after 3 weeks. The overshooting may come from hypertension and dilation of the blood vessel. In contrast, blood flow almost immediately stopped after laser-induced micro-hemorrhage insults, indicating a physical breach on the vessel so that the blood cannot flow through. In addition, the low level of blood flow never returned to normal thereafter (Figure 7b). Interestingly, the slow blood flow seems correlated with microglial aggregation around the targeted vessel in both scenarios, suggesting that microglia may participate in the down regulation of blood flow. In the case of mild ischemia, microglial activation preceded the decrease of blood flow, supporting that microglial activation might be leading to blood flow drop. However, these observations are based on small sample sizes. The exact causality relationship between microglial activation and blood flow speed reduction warrants further investigations.

4.4. Microglial degeneration

We noticed signs of microglial degeneration after the laser induced micro-hemorrhage. Right after the onset of hemorrhage, as the intravascular red fluorescent dye leaking out, surrounding CX3CR1-GFP signal quickly faded away in several minutes (Figure 7a, supplementary movie 4). The GFP dark region was much larger than the area that the leaked intravascular dye covered, indicating mechanisms other than the light absorption of the spilled blood. In addition, the remaining CX3CR1-GFP dots in the dark region became immobile, suggesting a dysfunction or fragmentation of microglia. Until other surrounding microglia later covered the dark region by migrating soma or extending processes in 30 min to 4 hours, no indication of recovery was found for those dysfunctional or fragmented microglia. The vasogenic edema around the insulted vessel indicates increased vascular permeability and leaking of blood components to the parenchyma, some of which may be toxic to the brain cells [6–8, 75]. In another case, we observed a microglia cell losing fluorescence near the micro-hemorrhage (50μm away) in ~10 min. From the 3D time lapse video, it was confirmed that the microglia cell did not migrate but just faded away (supplementary movie 4). Microglial degeneration and dysfunction have been associated with a variety of pathology. For example, microglial fragmentation (dystrophic microglia)

was found in the aging brain, Alzheimer's disease and Huntington's disease as well as near chronic neural implants[76–80]. Additionally, after ischemic stroke, the length and motility of microglia processes decrease in the peri-infarct region[50]. These studies are limited to postmortem histology or acute slice studies. Here, we revealed in the intact brain of live animals, a micro-hemorrhage can lead to microglia degeneration and dysfunction in a few minutes, suggesting that the blood brain barrier (BBB) impairment can be a direct cause of microglial degeneration and dysfunction, which may play an important role in the pathogenesis of neurodegeneration and neurovascular diseases.

4.5. Future applications

In vivo imaging studies can provide invaluable dynamic information of how biomaterials interact with the tissue in living organisms. However, chronic in vivo two-photon imaging of deep brain in the presence of neural implants has been extremely challenging due to the degradation of imaging quality and depth over time [15, 81, 82]. Hence previous in vivo imaging work on foreign body responses to neural electrodes have focused on acute phase and/or superficial cortex [7, 8, 75, 83]. Here we demonstrated the possibility of using microprism implantation for long-term in vivo imaging of inflammatory responses for the first time. This use enables easier access to deeper cortical or subcortical regions. While deeper regions can also be imaged by novel methods like three-photon microscopy [84, 85], microprisms still allow for higher resolution imaging in the vertical direction. This setup could be utilized to investigate the tissue responses to different neural implant materials in the brain by modifying the surface of microprisms. Furthermore, inserting functional microelectrodes next to the microprism or directly attaching flexible and transparent electrodes onto the microprism may allow us to correlate the electrophysiological signals and electrical modulations with cellular activities observed via two-photon imaging for longitudinal studies.

Two-photon microscopy is well suited for imaging genetically expressed fluorescent molecules and injected fluorophores, as well as intrinsic molecular signals such as NAD(P)H and second harmonic generation (SHG) of collagen [86–89]. In combination with microprism implantation, this imaging platform could reveal a variety of in vivo physiological processes along depth. For example, collagen rich encapsulation tissue around neural implants has been characterized via SHG signals in previous *in vivo* [83] and *ex vivo* [88, 90] two-photon imaging studies as part of the foreign body reaction. SHG signals could also be used to track the meningeal healing and collagen encapsulation near the microprism implant or collagen deposition at the site of microhemorrhage. This work builds the foundation for future explorations related with brain damage or neurodegenerative diseases using microprisms.

The dimension and configuration of microprism implant can be varied for different purposes. Microprisms of various sizes (0.5mm~5mm) are commercially available. Larger sizes of microprisms could provide access to deeper brain regions while potentially causing more severe damage to the tissue.

Inter-regional studies should benefit greatly from imaging different regions at various depth simultaneously, such as studies of inflammation responses and tissue remodeling in grey matter and underlying white matter.

5. Conclusion

In this work, we evaluated the inflammatory responses to intra-cortical microprism for 16 weeks, using in vivo two-photon imaging on awake animals. The imaging window is cleared of blood in about two weeks, and the imaging distance from the microprism face is stabilized at around 500 μm in about 5 weeks. The morphology and motility of microglia were characterized and compared with that from non-implant controls. Near the microprism face (50 μm), microglia recovered in 4~12 weeks, and more distant microglia returned to the homeostatic status faster. These results prove that chronic imaging through microprisms can be used for longitudinal inflammation-related studies after several weeks of recovery. Next, as a demonstration of the utility of this method, we characterized the inflammatory responses to laser induced micro-blood vessel insults on these microprism-implanted animals for another 16 weeks. Using microprism and in vivo two-photon microscopy, we found that laser-induced micro-hemorrhage led to widespread microglial polarization(~250μm) and fast-migration in the acute phase, and blood flow decreases and constant aggregations of microglia/macrophages around the insult in the long-term. In addition, we reported for the first time that micro-hemorrhage can result in microglial degeneration and that polarized microglial processes still have the potential to re-polarize to a new injury. This work paves the way for microprism implantations on long-term *in vivo* observations and evaluations of inflammatory responses, vascular remodeling, and other cellular activities from the brain surface to deep layer simultaneously.

Supplementary Material

Refer to Web version on PubMed Central for supplementary material.

Acknowledgement

The authors thank Dr. Takashi Kozai for providing two-photon imaging instruments. This research is financially supported by the NIH R01NS062019, R01NS089688 and R01NS110564.

7. Data availability

The raw/processed data required to reproduce these findings cannot be shared at this time as the data also forms part of ongoing studies.

References

[1]. Denk W, Strickler JH, Webb WW, Two-photon laser scanning fluorescence microscopy, Science248(4951) (1990) 73–76. [PubMed: 2321027]

[2]. Svoboda K, Denk W, Kleinfeld D, Tank DW, In vivo dendritic calcium dynamics in neocortical pyramidal neurons, Nature385(6612) (1997) 161–165. [PubMed: 8990119]

[3]. Stosiek C, Garaschuk O, Holthoff K, Konnerth A, In vivo two-photon calcium imaging of neuronal networks, Proceedings of the National Academy of Sciences100(12) (2003) 7319–7324.

[4]. Denk W, Delaney KR, Gelperin A, Kleinfeld D, Strowbridge B, Tank DW, Yuste R, Anatomical and functional imaging of neurons using 2-photon laser scanning microscopy, Journal of neuroscience methods54(2) (1994) 151–162. [PubMed: 7869748]

[5]. Davalos D, Grutzendler J, Yang G, Kim JV, Zuo Y, Jung S, Littman DR, Dustin ML, Gan W-B, ATP mediates rapid microglial response to local brain injury in vivo, Nature neuroscience8(6) (2005) 752–758. [PubMed: 15895084]

[6]. Kozai TDY, Vazquez AL, Weaver CL, Kim S-G, Cui XT, In vivo two-photon microscopy reveals immediate microglial reaction to implantation of microelectrode through extension of processes, Journal of neural engineering9(6) (2012) 066001. [PubMed: 23075490]

[7]. Eles JR, Vazquez AL, Snyder NR, Lagenaur C, Murphy MC, Kozai TD, Cui XT, Neuroadhesive L1 coating attenuates acute microglial attachment to neural electrodes as revealed by live two-photon microscopy, Biomaterials113 (2017) 279–292. [PubMed: 27837661]

[8]. Yang Q, Wu B, Eles J, Vazquez A, Kozai T, Cui X, Zwitterionic Polymer Coating Suppresses Microglial Encapsulation to Neural Implants In Vitro and In Vivo, Advanced Biosystems (2020) e1900287–e1900287. [PubMed: 32363792]

[9]. Svoboda K, Yasuda R, Principles of two-photon excitation microscopy and its applications to neuroscience, Neuron50(6) (2006) 823–839. [PubMed: 16772166]

[10]. Lückoff A, Scholz R, Sennlaub F, Xu H, Langmann T, Comprehensive analysis of mouse retinal mononuclear phagocytes, Nature protocols12(6) (2017) 1136–1150. [PubMed: 28471458]

[11]. Holtmaat A, Bonhoeffer T, Chow DK, Chuckowree J, De Paola V, Hofer SB, Hübener M, Keck T, Knott G, Lee W-CA, Long-term, high-resolution imaging in the mouse neocortex through a chronic cranial window, Nature protocols4(8) (2009) 1128. [PubMed: 19617885]

[12]. Yang G, Pan F, Parkhurst CN, Grutzendler J, Gan W-B, Thinned-skull cranial window technique for long-term imaging of the cortex in live mice, Nature protocols5(2) (2010) 201. [PubMed: 20134419]

[13]. Helmchen F, Svoboda K, Denk W, Tank DW, In vivo dendritic calcium dynamics in deep-layer cortical pyramidal neurons, Nature neuroscience2(11) (1999) 989–996. [PubMed: 10526338]

[14]. Hopt A, Neher E, Highly nonlinear photodamage in two-photon fluorescence microscopy, Biophysical journal80(4) (2001) 2029–2036. [PubMed: 11259316]

[15]. Kozai TD, Eles JR, Vazquez AL, Cui XT, Two-photon imaging of chronically implanted neural electrodes: Sealing methods and new insights, Journal of neuroscience methods258 (2016) 46–55. [PubMed: 26526459]

[16]. Wodlinger B, Downey J, Tyler-Kabara E, Schwartz A, Boninger M, Collinger J, Ten-dimensional anthropomorphic arm control in a human brain− machine interface: difficulties, solutions, and limitations, Journal of neural engineering12(1) (2014) 016011. [PubMed: 25514320]

[17]. Flesher SN, Collinger JL, Foldes ST, Weiss JM, Downey JE, Tyler-Kabara EC, Bensmaia SJ, Schwartz AB, Boninger ML, Gaunt RA, Intracortical microstimulation of human somatosensory cortex, Science translational medicine8(361) (2016) 361ra141–361ra141.

[18]. Simeral J, Kim S-P, Black M, Donoghue J, Hochberg L, Neural control of cursor trajectory and click by a human with tetraplegia 1000 days after implant of an intracortical microelectrode array, Journal of neural engineering8(2) (2011) 025027. [PubMed: 21436513]

[19]. Chia TH, Levene MJ, Microprisms for in vivo multilayer cortical imaging, Journal of neurophysiology102(2) (2009) 1310–1314. [PubMed: 19494189]

[20]. Andermann ML, Gilfoy NB, Goldey GJ, Sachdev RN, Wölfel M, McCormick DA, Reid RC, Levene MJ, Chronic cellular imaging of entire cortical columns in awake mice using microprisms, Neuron80(4) (2013) 900–913. [PubMed: 24139817]

[21]. Low RJ, Gu Y, Tank DW, Cellular resolution optical access to brain regions in fissures: imaging medial prefrontal cortex and grid cells in entorhinal cortex, Proceedings of the National Academy of Sciences111(52) (2014) 18739–18744.

[22]. Beckmann L, Zhang X, Nadkarni NA, Cai Z, Batra A, Sullivan DP, Muller WA, Sun C, Kuranov R, Zhang HF, Longitudinal deep-brain imaging in mouse using visible-light optical coherence tomography through chronic microprism cranial window, Biomedical optics express10(10) (2019) 5235–5250. [PubMed: 31646044]

[23]. Bessis A, Béchade C, Bernard D, Roumier A, Microglial control of neuronal death and synaptic properties, Glia55(3) (2007) 233–238. [PubMed: 17106878]

[24]. Piani D, Frei K, Do KQ, Cuénod M, Fontana A, Murine brain macrophages induce NMDA receptor mediated neurotoxicity in vitro by secreting glutamate, Neuroscience letters133(2) (1991) 159–162. [PubMed: 1687755]

[25]. Paolicelli RC, Bolasco G, Pagani F, Maggi L, Scianni M, Panzanelli P, Giustetto M, Ferreira TA, Guiducci E, Dumas L, Synaptic pruning by microglia is necessary for normal brain development, science333(6048) (2011) 1456–1458. [PubMed: 21778362]

[26]. Jolivel V, Bicker F, Binamé F, Ploen R, Keller S, Gollan R, Jurek B, Birkenstock J, Poisa-Beiro L, Bruttger J, Perivascular microglia promote blood vessel disintegration in the ischemic penumbra, Acta neuropathologica129(2) (2015) 279–295. [PubMed: 25500713]

[27]. Shih AY, Driscoll JD, Pesavento MJ, Kleinfeld D, Two-Photon Microscopy to Measure Blood Flow and Concurrent Brain Cell Activity, Optical Imaging of Neocortical Dynamics, Springer2014, pp. 273–290.

[28]. Kleinfeld D, Mitra PP, Helmchen F, Denk W, Fluctuations and stimulus-induced changes in blood flow observed in individual capillaries in layers 2 through 4 of rat neocortex, Proceedings of the National Academy of Sciences95(26) (1998) 15741–15746.

[29]. Jung S, Aliberti J, Graemmel P, Sunshine MJ, Kreutzberg GW, Sher A, Littman DR, Analysis of fractalkine receptor CX3CR1 function by targeted deletion and green fluorescent protein reporter gene insertion, Molecular and cellular biology20(11) (2000) 4106–4114. [PubMed: 10805752]

[30]. Geissmann F, Manz MG, Jung S, Sieweke MH, Merad M, Ley K, Development of monocytes, macrophages, and dendritic cells, Science327(5966) (2010) 656–661. [PubMed: 20133564]

[31]. Paschalis EI, Lei F, Zhou C, Kapoulea V, Thanos A, Dana R, Vavvas DG, Chodosh J, Dohlman CH, The role of microglia and peripheral monocytes in retinal damage after corneal chemical injury, The American journal of pathology188(7) (2018) 1580–1596. [PubMed: 29630857]

[32]. Nimmerjahn A, Kirchhoff F, Helmchen F, Resting microglial cells are highly dynamic surveillants of brain parenchyma in vivo, Science308(5726) (2005) 1314–1318. [PubMed: 15831717]

[33]. Ahn SJ, Anrather J, Nishimura N, Schaffer CB, Diverse inflammatory response after cerebral microbleeds includes coordinated microglial migration and proliferation, Stroke49(7) (2018) 1719–1726. [PubMed: 29844029]

[34]. Cao T, Thomas TC, Ziebell JM, Pauly JR, Lifshitz J, Morphological and genetic activation of microglia after diffuse traumatic brain injury in the rat, Neuroscience225 (2012) 65–75. [PubMed: 22960311]

[35]. Denes A, Vidyasagar R, Feng J, Narvainen J, McColl BW, Kauppinen RA, Allan SM, Proliferating resident microglia after focal cerebral ischaemia in mice, Journal of Cerebral Blood Flow & Metabolism27(12) (2007) 1941–1953. [PubMed: 17440490]

[36]. Polikov VS, Tresco PA, Reichert WM, Response of brain tissue to chronically implanted neural electrodes, Journal of neuroscience methods148(1) (2005) 1–18. [PubMed: 16198003]

[37]. Nishimura N, Schaffer CB, Friedman B, Tsai PS, Lyden PD, Kleinfeld D, Targeted insult to subsurface cortical blood vessels using ultrashort laser pulses: three models of stroke, Nature methods3(2) (2006) 99–108. [PubMed: 16432519]

[38]. Smith EE, Schneider JA, Wardlaw JM, Greenberg SM, Cerebral microinfarcts: the invisible lesions, The Lancet Neurology11(3) (2012) 272–282. [PubMed: 22341035]

[39]. Yang T-T, Lin C, Hsu C-T, Wang T-F, Ke F-Y, Kuo Y-M, Differential distribution and activation of microglia in the brain of male C57BL/6J mice, Brain Structure and Function218(4) (2013) 1051–1060. [PubMed: 22886465]

[40]. Lawson LJ, Perry VH, Dri P, Gordon S, Heterogeneity in the distribution and morphology of microglia in the normal adult mouse brain, Neuroscience39(1) (1990) 151–170. [PubMed: 2089275]

[41]. Shih AY, Blinder P, Tsai PS, Friedman B, Stanley G, Lyden PD, Kleinfeld D, The smallest stroke: occlusion of one penetrating vessel leads to infarction and a cognitive deficit, Nature neuroscience16(1) (2013) 55–63. [PubMed: 23242312]

[42]. Goldmann T, Wieghofer P, Jordão MJC, Prutek F, Hagemeyer N, Frenzel K, Amann L, Staszewski O, Kierdorf K, Krueger M, Origin, fate and dynamics of macrophages at central nervous system interfaces, Nature immunology17(7) (2016) 797. [PubMed: 27135602]

[43]. Saxena T, Karumbaiah L, Gaupp EA, Patkar R, Patil K, Betancur M, Stanley GB, Bellamkonda RV, The impact of chronic blood–brain barrier breach on intracortical electrode function, Biomaterials34(20) (2013) 4703–4713. [PubMed: 23562053]

[44]. Bennett C, Samikkannu M, Mohammed F, Dietrich WD, Rajguru SM, Prasad A, Blood brain barrier (BBB)-disruption in intracortical silicon microelectrode implants, Biomaterials164 (2018) 1–10. [PubMed: 29477707]

[45]. Kozai T, Marzullo T, Hooi F, Langhals N, Majewska A, Brown E, Kipke D, Reduction of neurovascular damage resulting from microelectrode insertion into the cerebral cortex using in vivo two-photon mapping, Journal of neural engineering7(4) (2010) 046011. [PubMed: 20644246]

[46]. Wellman SM, Kozai TD, In vivo spatiotemporal dynamics of NG2 glia activity caused by neural electrode implantation, Biomaterials164 (2018) 121–133. [PubMed: 29501892]

[47]. Golabchi A, Wu B, Li X, Carlisle DL, Kozai TD, Friedlander RM, Cui XT, Melatonin improves quality and longevity of chronic neural recording, Biomaterials180 (2018) 225–239. [PubMed: 30053658]

[48]. Kozai TD, Gugel Z, Li X, Gilgunn PJ, Khilwani R, Ozdoganlar OB, Fedder GK, Weber DJ, Cui XT, Chronic tissue response to carboxymethyl cellulose based dissolvable insertion needle for ultrasmall neural probes, Biomaterials35(34) (2014) 9255–9268. [PubMed: 25128375]

[49]. Young K, Morrison H, Quantifying microglia morphology from photomicrographs of immunohistochemistry prepared tissue using ImageJ, Journal of visualized experiments: JoVE (136) (2018).

[50]. Morrison HW, Filosa JA, A quantitative spatiotemporal analysis of microglia morphology during ischemic stroke and reperfusion, Journal of neuroinflammation10(1) (2013) 782.

[51]. Biran R, Martin DC, Tresco PA, Neuronal cell loss accompanies the brain tissue response to chronically implanted silicon microelectrode arrays, Experimental neurology195(1) (2005) 115–126. [PubMed: 16045910]

[52]. Potter-Baker KA, Ravikumar M, Burke AA, Meador WD, Householder KT, Buck AC, Sunil S, Stewart WG, Anna JP, Tomaszewski WH, A comparison of neuroinflammation to implanted microelectrodes in rat and mouse models, Biomaterials35(22) (2014) 5637–5646. [PubMed: 24755527]

[53]. Tomer R, Ye L, Hsueh B, Deisseroth K, Advanced CLARITY for rapid and high-resolution imaging of intact tissues, Nature protocols9(7) (2014) 1682–1697. [PubMed: 24945384]

[54]. Woolley AJ, Desai HA, Steckbeck MA, Patel NK, Otto KJ, In situ characterization of the brain–microdevice interface using device capture histology, Journal of neuroscience methods201(1) (2011) 67–77. [PubMed: 21802446]

[55]. Klatzo I, Pathophysiological aspects of brain edema, Acta neuropathologica72(3) (1987) 236–239. [PubMed: 3564903]

[56]. Unterberg A, Stover J, Kress B, Kiening K, Edema and brain trauma, Neuroscience129(4) (2004) 1019–1027.

[57]. Tremblay M-È, Lecours C, Samson L, Sánchez-Zafra V, Sierra A, From the Cajal alumni Achúcarro and Río-Hortega to the rediscovery of never-resting microglia, Frontiers in neuroanatomy9 (2015) 45. [PubMed: 25926775]

[58]. Raivich G, Bohatschek M, Kloss CU, Werner A, Jones LL, Kreutzberg GW, Neuroglial activation repertoire in the injured brain: graded response, molecular mechanisms and cues to physiological function, Brain research reviews30(1) (1999) 77–105. [PubMed: 10407127]

[59]. Stence N, Waite M, Dailey ME, Dynamics of microglial activation: A confocal time-lapse analysis in hippocampal slices, Glia33(3) (2001) 256–266. [PubMed: 11241743]

[60]. Kreutzberg GW, Microglia: a sensor for pathological events in the CNS, Trends in neurosciences19(8) (1996) 312–318. [PubMed: 8843599]

[61]. Chiu IM, Morimoto ET, Goodarzi H, Liao JT, O'Keeffe S, Phatnani HP, Muratet M, Carroll MC, Levy S, Tavazoie S, A neurodegeneration-specific gene-expression signature of acutely isolated

microglia from an amyotrophic lateral sclerosis mouse model, Cell reports4(2) (2013) 385–401. [PubMed: 23850290]

[62]. Wes PD, Holtman IR, Boddeke EW, Möller T, Eggen BJ, Next generation transcriptomics and genomics elucidate biological complexity of microglia in health and disease, Glia64(2) (2016) 197–213. [PubMed: 26040959]

[63]. Hu X, Li P, Guo Y, Wang H, Leak RK, Chen S, Gao Y, Chen J, Microglia/macrophage polarization dynamics reveal novel mechanism of injury expansion after focal cerebral ischemia, Stroke43(11) (2012) 3063–3070. [PubMed: 22933588]

[64]. Ravikumar M, Sunil S, Black J, Barkauskas DS, Haung AY, Miller RH, Selkirk SM, Capadona JR, The roles of blood-derived macrophages and resident microglia in the neuroinflammatory response to implanted intracortical microelectrodes, Biomaterials35(28) (2014) 8049–8064. [PubMed: 24973296]

[65]. Jones JR, Gentleman E, Polak J, Bioactive glass scaffolds for bone regeneration, Elements3(6) (2007) 393–399.

[66]. Weinstein A, Klawitter J, Cook S, Implant-bone interface characteristics of bioglass dental implants, Journal of biomedical materials research14(1) (1980) 23–29. [PubMed: 6987233]

[67]. Song E-C, Chu K, Jeong S-W, Jung K-H, Kim S-H, Kim M, Yoon B-W, Hyperglycemia exacerbates brain edema and perihematomal cell death after intracerebral hemorrhage, Stroke34(9) (2003) 2215–2220. [PubMed: 12907821]

[68]. Grysiewicz RA, Thomas K, Pandey DK, Epidemiology of ischemic and hemorrhagic stroke: incidence, prevalence, mortality, and risk factors, Neurologic clinics26(4) (2008) 871–895. [PubMed: 19026895]

[69]. Rosamond WD, Folsom AR, Chambless LE, Wang C-H, McGovern PG, Howard G, Copper LS, Shahar E, Stroke incidence and survival among middle-aged adults: 9-year follow-up of the Atherosclerosis Risk in Communities (ARIC) cohort, Stroke30(4) (1999) 736–743. [PubMed: 10187871]

[70]. Taylor RA, Sansing LH, Microglial responses after ischemic stroke and intracerebral hemorrhage, Clinical and Developmental Immunology2013 (2013).

[71]. Rosidi NL, Zhou J, Pattanaik S, Wang P, Jin W, Brophy M, Olbricht WL, Nishimura N, Schaffer CB, Cortical microhemorrhages cause local inflammation but do not trigger widespread dendrite degeneration, PLoS One6(10) (2011) e26612. [PubMed: 22028924]

[72]. Bernick C, Kuller L, Dulberg C, Longstreth W Jr, Manolio T, Beauchamp N, Price T, Silent MRI infarcts and the risk of future stroke: the cardiovascular health study, Neurology57(7) (2001) 1222–1229. [PubMed: 11591840]

[73]. Vermeer SE, Hollander M, van Dijk EJ, Hofman A, Koudstaal PJ, Breteler MM, Silent brain infarcts and white matter lesions increase stroke risk in the general population: the Rotterdam Scan Study, Stroke34(5) (2003) 1126–1129. [PubMed: 12690219]

[74]. Rosenblum WI, El-Sabban F, Platelet aggregation in the cerebral microcirculation: effect of aspirin and other agents, Circulation Research40(3) (1977) 320–328. [PubMed: 13943]

[75]. Lee KR, Kawai N, Kim S, Sagher O, Hoff JT, Mechanisms of edema formation after intracerebral hemorrhage: effects of thrombin on cerebral blood flow, blood-brain barrier permeability, and cell survival in a rat model, Journal of neurosurgery86(2) (1997) 272–278. [PubMed: 9010429]

[76]. Streit WJ, Braak H, Xue Q-S, Bechmann I, Dystrophic (senescent) rather than activated microglial cells are associated with tau pathology and likely precede neurodegeneration in Alzheimer's disease, Acta neuropathologica118(4) (2009) 475–485. [PubMed: 19513731]

[77]. Streit WJ, Sammons NW, Kuhns AJ, Sparks DL, Dystrophic microglia in the aging human brain, Glia45(2) (2004) 208–212. [PubMed: 14730714]

[78]. Simmons DA, Casale M, Alcon B, Pham N, Narayan N, Lynch G, Ferritin accumulation in dystrophic microglia is an early event in the development of Huntington's disease, Glia55(10) (2007) 1074–1084. [PubMed: 17551926]

[79]. Lopes KO, Sparks DL, Streit WJ, Microglial dystrophy in the aged and Alzheimer's disease brain is associated with ferritin immunoreactivity, Glia56(10) (2008) 1048–1060. [PubMed: 18442088]

[80]. Prasad A, Xue Q-S, Sankar V, Nishida T, Shaw G, Streit WJ, Sanchez JC, Comprehensive characterization and failure modes of tungsten microwire arrays in chronic neural implants, Journal of neural engineering9(5) (2012) 056015. [PubMed: 23010756]

[81]. Haynes SE, Hollopeter G, Yang G, Kurpius D, Dailey ME, Gan W-B, Julius D, The P2Y 12 receptor regulates microglial activation by extracellular nucleotides, Nature neuroscience9(12) (2006) 1512–1519. [PubMed: 17115040]

[82]. Ohsawa K, Irino Y, Sanagi T, Nakamura Y, Suzuki E, Inoue K, Kohsaka S, P2Y12 receptor-mediated integrin-β1 activation regulates microglial process extension induced by ATP, Glia58(7) (2010) 790–801. [PubMed: 20091784]

[83]. Eles J, Vazquez A, Kozai T, Cui X, Meningeal inflammatory response and fibrous tissue remodeling around intracortical implants: an in vivo two-photon imaging study, Biomaterials195 (2019) 111–123. [PubMed: 30634095]

[84]. Horton NG, Wang K, Kobat D, Clark CG, Wise FW, Schaffer CB, Xu C, In vivo three-photon microscopy of subcortical structures within an intact mouse brain, Nature photonics7(3) (2013) 205–209.

[85]. Hontani Y, Xia F, Xu C, Multicolor three-photon fluorescence imaging with single-wavelength excitation deep in mouse brain, Science Advances7(12) (2021) eabf3531. [PubMed: 33731355]

[86]. Zipfel WR, Williams RM, Christie R, Nikitin AY, Hyman BT, Webb WW, Live tissue intrinsic emission microscopy using multiphoton-excited native fluorescence and second harmonic generation, Proceedings of the National Academy of Sciences100(12) (2003) 7075–7080.

[87]. Kwan AC, Duff K, Gouras GK, Webb WW, Optical visualization of Alzheimer's pathology via multiphoton-excited intrinsic fluorescence and second harmonic generation, Optics express17(5) (2009) 3679–3689. [PubMed: 19259208]

[88]. Esquibel CR, Wendt KD, Lee HC, Gaire J, Shoffstall A, Urdaneta ME, Chacko JV, Brodnick SK, Otto KJ, Capadona JR, Second Harmonic Generation Imaging of Collagen in Chronically Implantable Electrodes in Brain Tissue, Frontiers in Neuroscience14 (2020) 95. [PubMed: 32733179]

[89]. Zoumi A, Yeh A, Tromberg BJ, Imaging cells and extracellular matrix in vivo by using second-harmonic generation and two-photon excited fluorescence, Proceedings of the National Academy of Sciences99(17) (2002) 11014–11019.

[90]. Degenhart AD, Eles J, Dum R, Mischel JL, Smalianchuk I, Endler B, Ashmore RC, Tyler-Kabara EC, Hatsopoulos NG, Wang W, Histological evaluation of a chronically-implanted electrocorticographic electrode grid in a non-human primate, Journal of neural engineering13(4) (2016) 046019. [PubMed: 27351722]

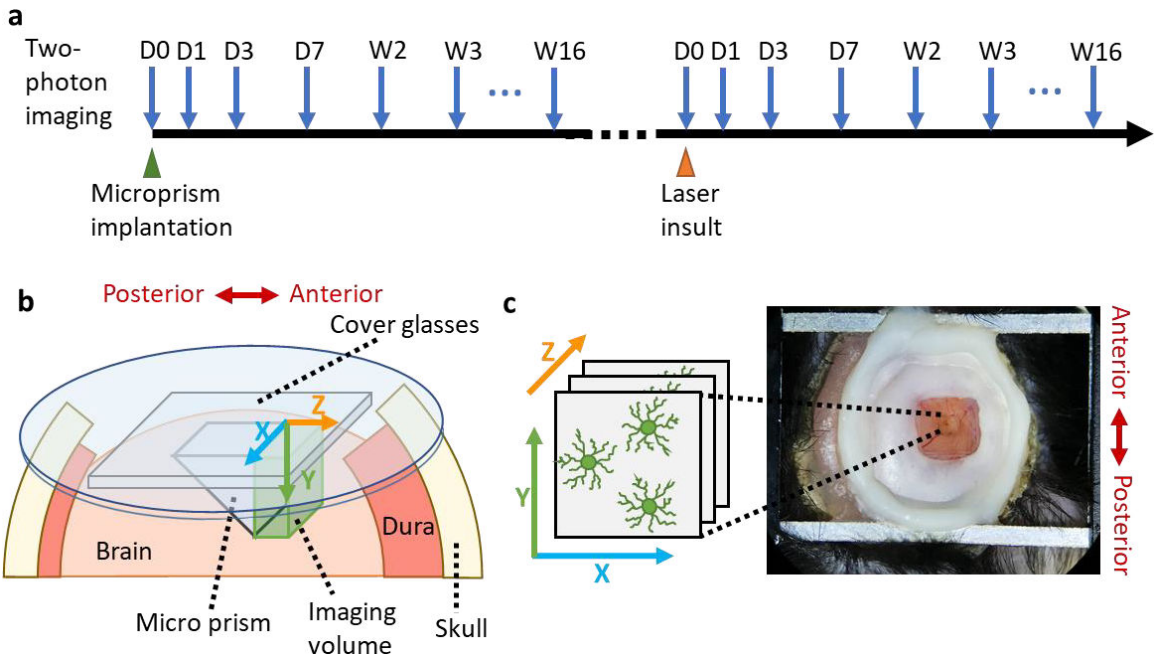

Figure 1. Experiment procedure and imaging setup

(a) Experimental procedure. Two-photon images were taken at the day of microprism implantation surgery, 1-day post implantation (DPI), 3 DPI, 7 DPI and then weekly for 16 weeks. Later, micro blood vessel insults were induced by point laser ablation. The surrounding brain tissue were imaged at the day of injury, day1, day3, day7 and then weekly for 16 weeks. (b) Schematic of the micro-prism device implanted in the cortex. Microprism was adhered to two square cover glass (3×3mm) and one round cover glass (5mm in diameter) and was inserted facing the anterior side. (c) Top view of the 3×3mm cranial window and metal frame on the head of mouse. Note the orientation of images taken through the 1mm microprism is upside down due to the reflection of the microprism.

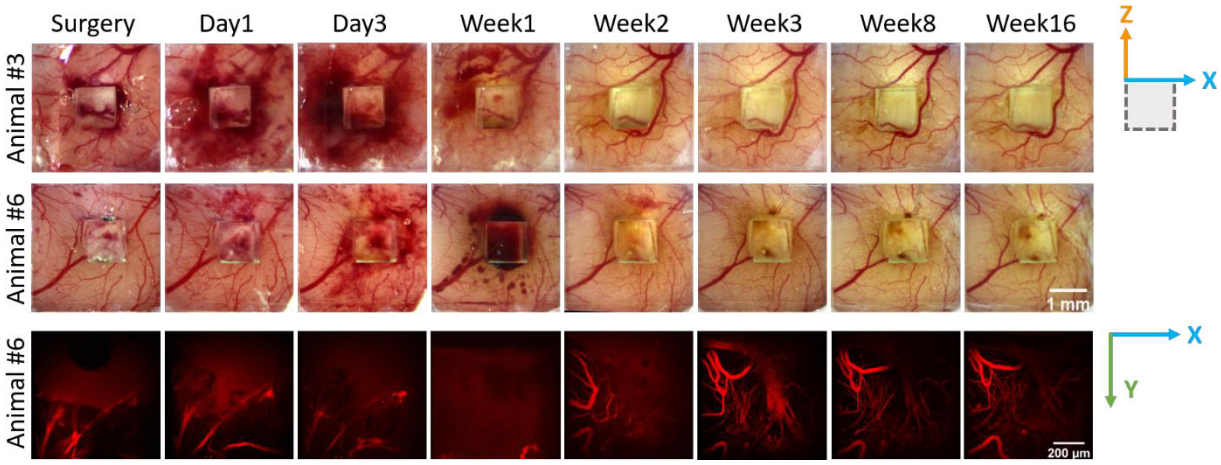

Figure 2. Vasculature remodeling after micro-prism implantation

Top two rows: representative wide field images of vasculatures at brain surface from two animals. Bottom row: representative 2-photon images of vasculatures as labeled in red (SR101) at the surface of micro-prism. Note that the vascular structure stabilized after week 3.

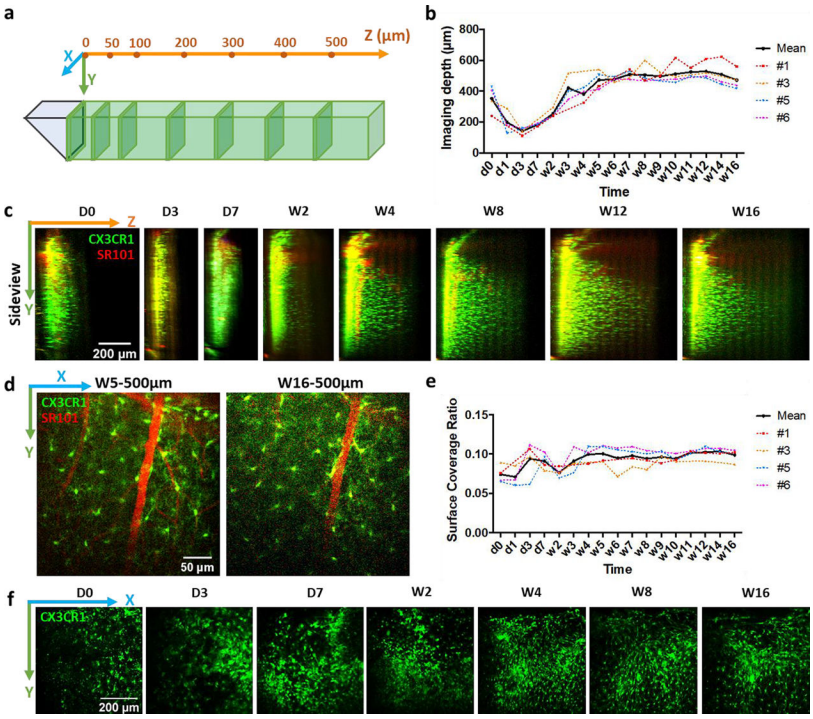

Figure 3. Image clarity after microprism implantations

(a) Schematics of imaging configuration. Following two-photon images are projected from thin slices (30 μm thick) at a series of z locations. (b) Measurements of maximum imaging distance in the Z direction over time. Colored lines represent animal #1, #3, #5 and #6 in (b) and (e). (c) Representative side-projections of two-photon image stacks at different time points after microprism implantations. Green: CX3CR1-GFP; Red: intravascular dye (SR101). (d) Representative two-photon images showing microglia (green) and vasculature (red) at 500μm from microprism surface at week5 and week16 post implantation. (e) Characterization of coverage ratio by CX3CR1-GFP cells at microprism surface. (f) Representative two-photon images at microprism surface showing the change of microglia/macrophage coverage in one animal over time.

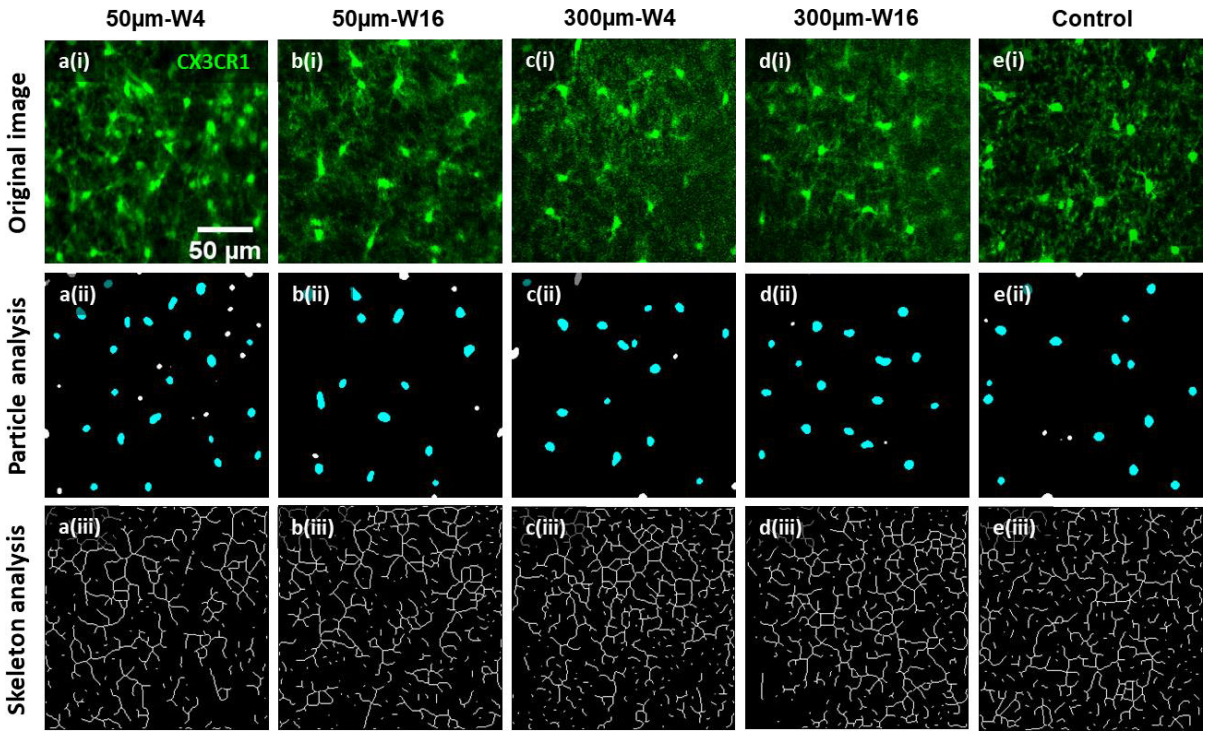

Figure 4. Representative microglial morphology and graphical analysis results after chronic microprism implantations

First row: representative two-photon images of microglia at 5μm (a(i) & b(i)) and 300μm (c(i) & d(i)) from the microprism surface and at week4 (a(i) & c(i)) and week16 (b(i) & d(i)) post microprism implantation. Representative control image (e(i)) is taken immediately after creation of acute craniotomy. Green: CX3CR1-GFP. Images in the same column are originated from the same image. The second row are particle analysis of images in the first row for microglial soma quantifications (soma density and area in figure 5). Cyan particles are counted for cell soma analysis, while the white particles are excluded because of undersize or incomplete shape (on the edges). The third row are skeleton analysis of images in the first row for quantification of microglial processes (processes length and junction numbers in figure 5). Notice that only the images at 50μm and week4 show obvious higher density, smaller soma, shorter processes, and less processes junctions of microglia compared to controls of acute craniotomy. Microglia at later time point (50μm-W16) or at distant regions (300μm-W4 & 300μm-W16) appear similar to the control.

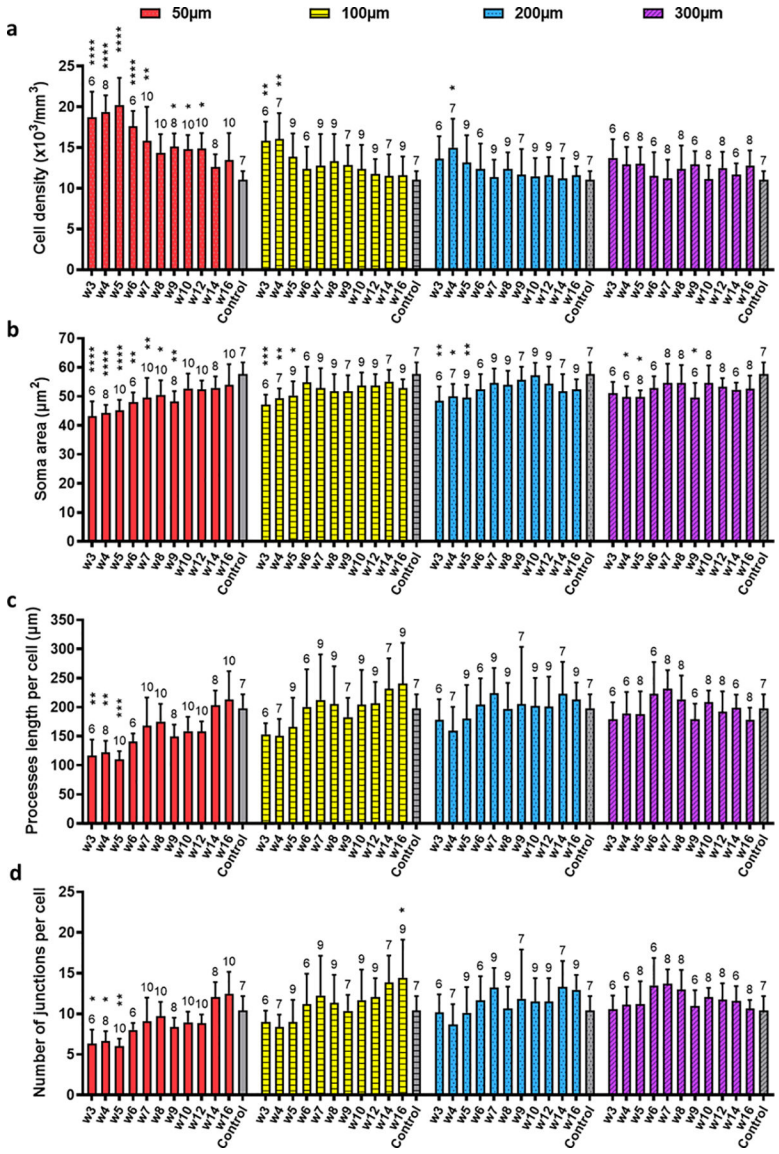

Figure 5. Quantification of microglial morphology after microprism implantation in comparison to non-implanted control.

(a) Quantifications of microglial density based on particle analysis. Control: acute non-implant craniotomy. Two-way ANOVA suggests that the two factors—time after implantation and distance from the microprism—both significantly affect the microglial density ($p<0.0001$), and there is an interaction effect ($p=0.0186$). Dunnett's multiple comparisons which compare every time point to the control within each distance reveal significant higher microglial density at multiple early time points at 50μm, week3 and week4 at 100μm, and week4 at 200μm than the acute craniotomy control. For all the panels in this figure, *: $p<0.05$, **: $p<0.01$, ***: $p<0.001$, ****: $p<0.0001$, the unmarked bars are not significantly different from the control. N=6~10 regions (200 × 200 μm^2 each) analyzed in each group from 4 animals for both the microprism implanted and the control. The exact number of regions analyzed are shown above each bar. Data are presented as mean ± SD.

(b) Quantifications of projected area of microglial soma based on particle analysis. The same

two-way ANOVA followed by Dunnett's multiple comparisons is used in (a)~(d). The time factor and the distance factor are significant ($p<0.0001$), while the interaction of these two factors is not ($p=0.5056$). In the post-hoc tests, the soma size from week3 to week9 at 50μm are significantly smaller than the control, as well as week3 to week5 at 100μm and 200μm, and week4, 5, 9 at 300μm. (c) Quantifications of average processes length per cell. The time factor and the distance factor are significant ($p<0.0001$), while the interaction of these two factors is not ($p=0.1932$). (d) Quantifications of processes junctions per cell. The time factor and the distance factor are significant ($p<0.0001$), while the interaction of these two factors is not ($p=0.0575$).

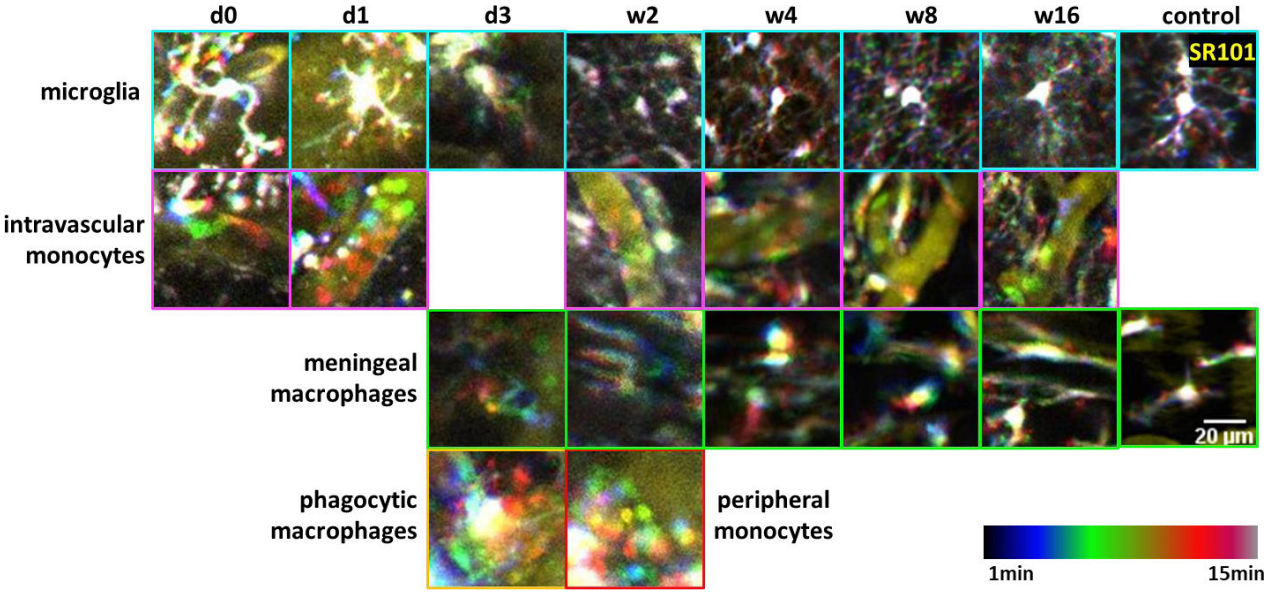

Figure 6. Morphology and dynamics of different types of CX3CR1-GFP cells over time

Representative temporal-code two-photon images of different types of CX3CR1^{+} cells at 50μm from the prism surface. Yellow: intravascular dye (SR101). Rainbow spectrum: temporal code of 15 min. Control images were from a non-implant thin skull CX3CR1-GFP mouse. First row (cyan outline): microglia became activated with enlarged cell body and shortened processes in the first several days post implant, and that ramified microglia with thin and motile processes and small soma returned around w2 to w4. Second row (magenta outline): small and round monocytes circulating in the blood vessels after microprism implantations. Third row (green outline): meningeal macrophages were absent at the beginning due to the removal of meninges. They appealed back at 3 DPI and lined up at the brain surface since w2. Forth row: giant foam-like phagocytic cells showed up from ~3 DPI and disappeared after w2 (yellow outline). Small and round monocytes were found wandering in the peripheral corticospinal fluid space around w2 (red outline).

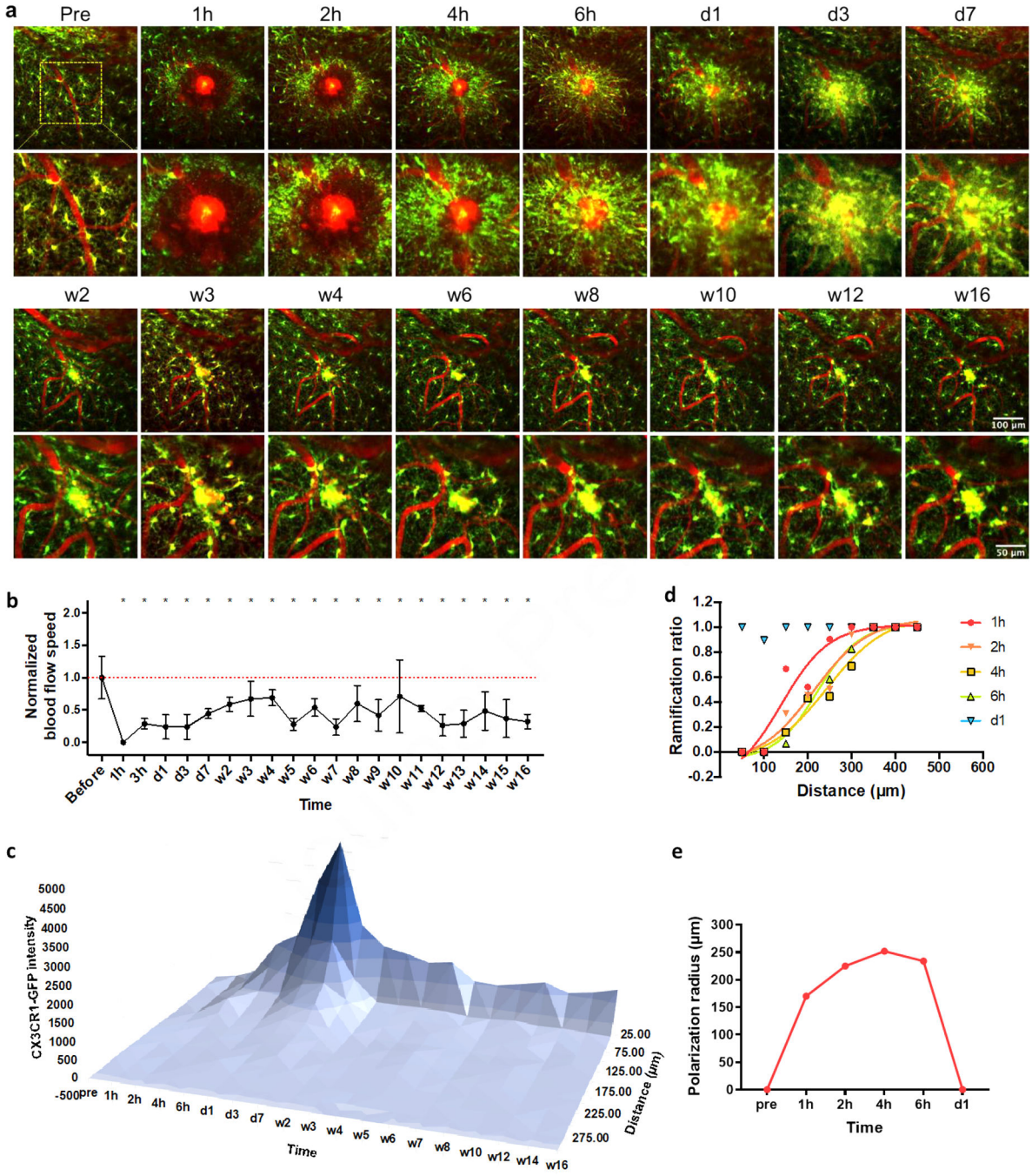

Figure 7. Prolonged microglia activation to micro-blood vessel hemorrhage

(a) Representative images at the damage plane overtime. Green: CX3CR1-GFP; Red: SR101. (b) Blood flow stopped quickly and remained significant lower post hemorrhage. One-way ANOVA followed by Dunnett's multiple comparisons test comparing every time point to pre-insult group. Data were presented as mean ± SD. N=6 to16 measurements from two biological replications. (c) Microglia intensity stayed high around damaged site over 16 weeks. Data were presented as the mean value from two biological replications. (d) Ramified microglia ratio over distance to the insult. Lines: Boltzmann sigmoidal fitting to

the ramification ratio of pooled microglia from two biological replications. (e) Polarization radios (the distance where the ramification ratio reaches 0.5 in the sigmoidal fitting) changes over time.

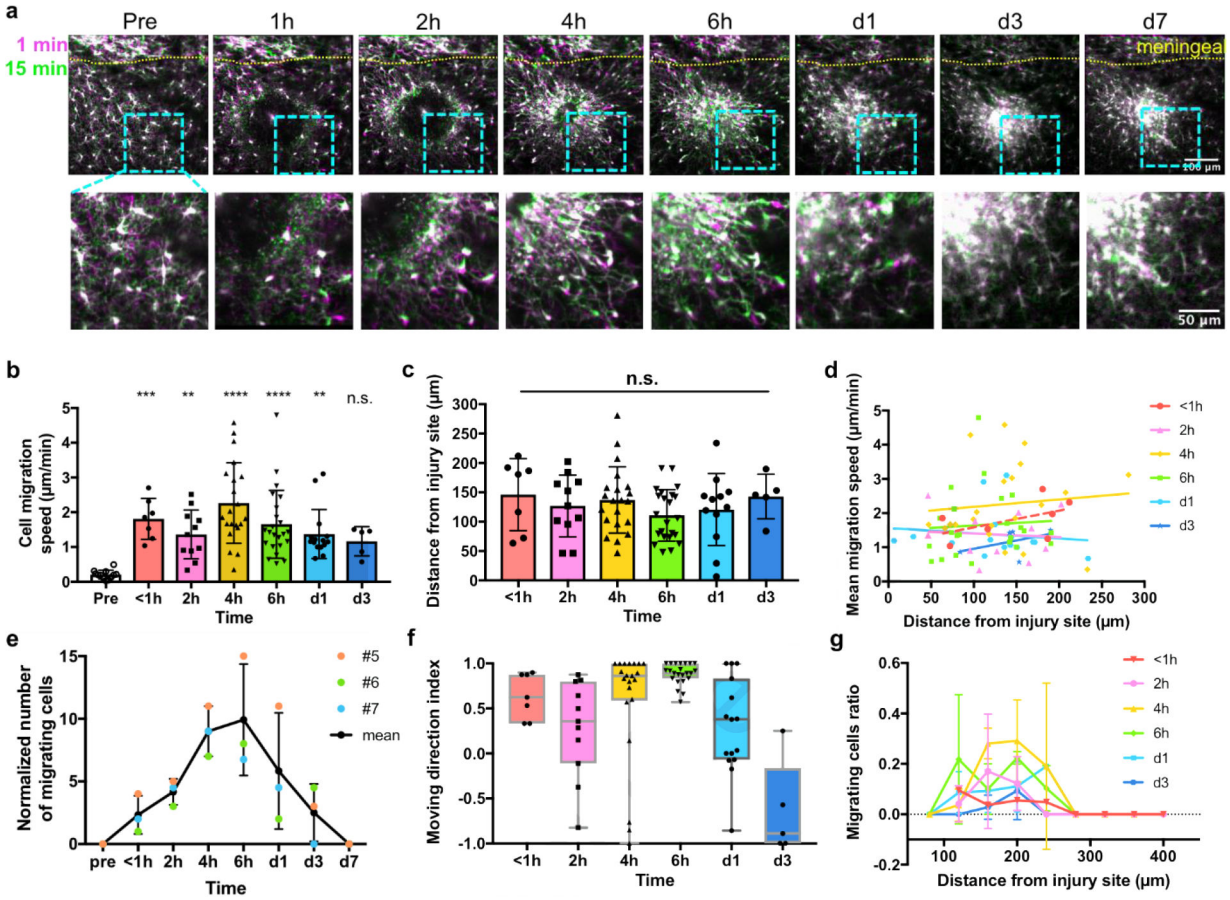

Figure 8. Microglial migration in the first week post micro-blood vessel hemorrhage

(a) Dynamics of CX3CR1-GFP cells post hemorrhage injury. Magenta: the first frame of the time-lapse images; green: 15 min later. Lower row: magnified image of the light blue inset above. (b) Migration speed of microglia before and after the hemorrhage. One-way ANOVA followed by Dunn's multiple comparisons test comparing every time points to the pre-insult group. N=12, 7, 11, 21, 23, 15 and 5 cells in time sequence from 3 animals for (b)~(f). (c) The distance between each migrating microglia and the injury site. One-way ANOVA, n.s.: no significance. (d) Microglial migration speed is independent from the distance from the injury site. Lines: linear regression fitting. All the slopes were not significantly different from zero (p=0.2403, 0.8282, 0.6510, 0.7681, 0.6681, 0.4616, respectively). (e) The number of migrating CX3CR1-GFP cells in the same imaging view over time. #5, #6, and #7: animal labels. Data were presented as mean ± SD. (f) The mean moving direction index of migrated cells. Boxes presented median ± quartile and whiskers covered min to max. (g) The ratio of migrating cells in all microglia over distance from the insult. Data were presented as mean ± SD. N=1 to 3 calculated ratios from 3 animals.